Dynamic modeling of interactions between shallow slow-slip events and subduction earthquakes

Qingjun Meng^{1*}, Benchun Duan¹

(1) Center of Tectonophysics, Department of Geology & Geophysics, Texas A&M University, College Station, TX 77843, United States

Qingjun Meng

E-mail: qimeng@tamu.edu

Declaration of Competing Interests

The authors acknowledge there are no conflicts of interest recorded.

Revised for publication in Seismological Research Letters.

Abstract:

1

2

3

4

5

6

7

8

9

10

11

12

13

14

15

16

17

18

19

20

21

22

23

Shallow slow slip events (SSEs) contribute to strain release near the shallow portions of subduction interfaces and may contribute to promoting shallow subduction earthquakes. Recent efforts in off-shore monitoring of shallow SSEs have provided evidence of possible interactions between shallow SSEs and megathrust earthquakes. In this study, we use a dynamic earthquake simulator that captures both quasi-static (for SSEs) and dynamic (for megathrust earthquakes) slip to explore their interactions and implications for seismic and tsunami hazards. We model slip behaviors of a shallowdipping subduction interface on which two locally locked patches (asperities) with different strengths are embedded within a conditionally stable zone. We find that both SSEs and earthquakes can occur, and they interact over multiple earthquake cycles in the model. Dynamic ruptures can nucleate on the asperities and propagate into the surrounding conditionally stable zone at slow speeds, generating tsunami earthquakes. A clear correlation emerges between the size of an earthquake and SSE activities preceding it. Small earthquakes rupture only the low-strength asperity, while large earthquakes rupture both. Before a large earthquake, periodic SSEs occur around the high-strength asperity, gradually loading stress into its interior. The critically stressed high-strength asperity can be ruptured together with the low-strength one in the large earthquake, followed by a relatively quiet interseismic period with very few SSEs and then a small earthquake. An SSE may or may not directly lead to nucleation of an earthquake, depending on whether a nearby asperity is ready for spontaneously dynamic failure. In addition, because of different SSE activities, the coupling degree may change dramatically between different interseismic periods, suggesting its estimate based on a short period of observation may be biased.

1. Introduction:

26

27

28

29

30

31

32

33

34

35

36

37

38

39

40

41

42

43

44

45

46

47

48

49

50

Since their discovery on the San Andreas fault in California (Linde et al., 1996), Southwest Japan (Hirose et al., 1999) and Cascadia (Dragert et al., 2001), slow slip events (SSEs) have been widely observed along subduction zones, for example in Guerrero (Lowry et al., 2001), Hikurangi (Douglas et al., 2005), Central Ecuador (Vallee et al., 2013), Northern Chile (Ruiz et al., 2014), central and northern Japan (Ozawa et al., 2003) and other places. Compared with regular earthquakes, SSEs have much slower rupture speeds (from about 6 km/day in Cascadia, Dragert et al., 2001, to about 2 km/day in Mexico, Franco et al., 2005), slip rates (from about 3 cm/year in the Bungo Channel, Japan, to about 1 m/year in Cascadia) and much longer duration (from 10 days in Cascadia to about 12 months in Mexico). Their relationships with regular earthquakes are complex and not fully understood. Some studies report that SSEs occurred before some large megathrust earthquakes and speculate SSEs may have triggered these earthquakes. For example, SSE occurred one month before the 2011 Mw 9.0 Tohoku-Oki earthquake and located within the huge coseismic-slip area of the mainshock (Kato et al., 2010; Ito et al., 2013), demonstrating that faults experiencing SSE can rupture seismically. Aseismic slip also occurred half a month before the 2014 Mw 8.1 Iquique earthquake, with the slip zone largely overlapped with the megathrust coseismic slip zone (Ruiz et al., 2014). Other studies suggest that SSEs could be triggered by seismic waves or static stress transfer of large earthquakes (Wallace et al., 2017; Hirose et al., 2012). However, SSEs may also occur without obvious interactions with megathrust earthquakes. For example, the periodic SSEs were found to occur every 11-18 months along the Cascadia subduction zone downdip of the seismogenic zone (Dragert et al, 2001; Szeliga et al., 2008), while no megathrust earthquakes have occurred in recent decades. Other slow-slip phenomena usually accompany with the 51 occurrence of SSEs, such as tremors, very low frequency events (VLFEs), low 52 frequency events (LFEs) and seismic swarms (Rogers and Dragert, 2003; Ito et al., 2007; Ghosh et al., 2015; Ozawa et al., 2007), even though the seismic moments released by 53 54 them only compose a very small portion of the moment released by the SSEs (Ito et al, 2009; Kao et al., 2009; Ozawa et al., 2007). 55 56 Early studies show that SSEs usually occur on the deep portion (30-50km depth) of 57 subduction zones near the base of the seismogenic depth (Dragert, 2001; Obara, 2002; 58 Peng and Gomberg, 2010). Though shallow SSEs are difficult to study due to their off-59 shore locations, more recent observations demonstrate that SSEs also occur at much 60 shallower depth near the trench along many subduction zones, including the Hikurangi Margin (Wallace et al., 2012), the North Japan Margin (Ito et al., 2013), the Costa Rican 61 62 Margin (Dixon et al., 2014) and other regions. Although most of the observed shallow 63 SSEs are smaller in magnitude compared with deep SSEs, they contribute much to the 64 strain release at the shallow portion of subduction zones. By studying and comparing 65 several shallow SSEs, Saffer and Wallace (2015) proposed that shallow SSEs, similar to deep SSEs, appear to occur along the severely overpressured zone coupled with the 66 67 frictional properties of clay minerals and a heterogeneous fault interface. Such a physical condition on subduction zone interfaces may also be favorable for hosting 68 69 shallow tsunami earthquakes. Tsunami earthquakes usually have much longer duration, 70 slower rupture speed (<1.5 km/s) and depleted high frequency radiation energy, 71 compared with deeper megathrust earthquakes, and they could generate larger tsunami 72 waves than their Ms magnitude implies (Kanamori, 1972; Kanamori and Kikuchi, 73 1993; Abercrombie et al., 2001; Ammon et al., 2006). Tsunami earthquakes have been linked with transitional friction properties on fault interfaces (Bilek and Lay, 2002; 74 Meng et al., 2022), which is also an essential factor for shallow SSE formation 75

(Kodaira, 2004; Liu and Rice, 2005). In the north Hikurangi margin, where shallow SSEs have been well studied, Barker et al. (2018) found that the slip area of the September-October 2014 shallow SSE contacts with two shallow subducting seamounts, which have been postulated as the epicenters of the two tsunami earthquakes occurred in this region in 1947 (Bell et al., 2014). Considering the subduction zone observations where SSEs occur within the coseismic slip zone preceding large earthquakes (Ito et al., 2013; Ruiz et al., 2014), we propose that shallow SSEs may play an important role for modulating the timing, size and characteristics of shallow subduction zone earthquakes, especially for tsunami earthquakes, at least along some subduction zones.

Some previous numerical simulations have explored megathrust earthquake rupture patterns over multiple earthquake cycles (e.g., Kaneko et al, 2010; Noda and Lapusta, 2013; Noda et al., 2021). Many other previous numerical simulations focus on exploring the subduction zone SSE activities (Liu and Rice, 2005; Segall et al. 2010; Li and Liu, 2016; Wei et al., 2018). However, few numerical studies have explored the interactions between shallow SSEs and megathrust earthquakes over earthquake cycles. Recently, Shibazako et al. (2019) make use of elastostatic kernels and radiation damping method to perform a quasi-dynamic analysis for modeling the long- and short-term SSEs and seismic events along the Hikurangi subduction zone. However, compared with fully-dynamic simulations, the quasi-dynamic calculation ignores the inertial wave-mediated effects during an earthquake and the simulated earthquakes have much smaller slip rate, rupture speed and recurrence interval than those simulated using fully-dynamic simulations (Napusta and Liu, 2009; Thomas et al., 2014). In this study, we use a fully dynamic earthquake cycle simulator that captures both quasi-static (for SSEs) and dynamic (for earthquakes) slip behaviors, and study the interactions

between the shallow SSEs and shallow subduction zone earthquakes. We incorporate a rate-and state-dependent friction law on a fault interface and apply heterogeneous friction and effective normal stress properties. In our models, unstable asperities (for earthquake nucleation) are embedded in a shallow conditionally stable zone (for hosting SSEs). Our simulation results may provide a reference to the less studied shallow subduction zone aseismic and seismic activities and their interactions, and improve tsunami hazard assessment using shallow SSEs, complementing recent efforts in seafloor geodesy to monitor shallow subduction interfaces.

2. Method and Model:

In this study, we use a fully dynamic earthquake simulator (Luo et al., 2020; Meng et al., 2022) to simulate slip behavior on a shallow-dipping subduction interface over multiple earthquake cycles. The dynamic simulator is based on an explicit finite element method (FEM) code EQdyna that has been developed for dynamic rupture simulations (Duan and Oglesby, 2006; Duan and Day, 2008; Duan, 2010; Duan, 2012; Luo and Duan, 2018; Liu and Duan, 2018). The simulator directly uses EQdyna for the coseismic dynamic process while integrates an adaptive dynamic relaxation technique (Qiang, 1988) and a variable time stepping scheme (Lapusta et al., 2000) with EQdyna to simulate the quasi-static processes, including the postseismic, interseismic, and nucleation phases. In this way, both the dynamic and quasi-static processes can be modeled in one FEM framework. On the plate interface, we adopt the rate-and state-dependent friction (RSF) law with aging law (Dieterich, 1979), which is commonly used for earthquake cycle simulations (e.g., Yu et al., 2018; Erickson and Dunham,

2014; Lapusta and Liu, 2009; Lapusta et al., 2000) and SSE cycle models (e.g. Liu and Rice, 2005; Segall et al. 2010; Li and Liu, 2016), as shown in the equations below:

127
$$\tau = \overline{\sigma}_n * (f_0 + a \ln \frac{v}{v_0} + b \ln \frac{v_0 \theta}{L})$$
 (1)

$$\frac{d\theta}{dt} = 1 - \frac{V\theta}{L} \tag{2}.$$

129

130

131

132

133

134

135

136

137

138

139

140

141

142

143

144

145

146

147

148

The frictional strength au is a function of effective normal stress $\bar{\sigma}_n$, reference slip rate V_0 , slip rate V , reference friction coefficient f_0 , state variable θ and characteristic slip distance L, as shown in equation (1). The coefficients of a and b represent the ratedependency and the state-dependency of the frictional strength, where a-b<0 means velocity weakening and a-b>0 represents velocity strengthening. In the aging law, the state variable θ evolves as a function of V, θ and L, as shown in equation (2). We set up a 3D thrust model with dipping angle $\phi = 30^{\circ}$, and the thrust fault plane intersects the free surface (Figure 1). For the quasi-static simulation, the top boundary of the model is the free surface, the left and right boundaries of the model are fixed along the strike direction (x direction), and a relative loading rate $0.5*V_{pl}$ is assigned on other boundaries so that the hanging wall moves upward and the footwall moves downward, parallel to the fault plane. We set V_{pl} as 10^{-9} m/s in this study. For the dynamic simulation, the top boundary is set as free surface and all other boundaries adopt perfectly matched layers (PML) to absorb seismic waves and minimize waveform reflection on the truncated model boundaries (Liu and Duan, 2018). We use a mesh size of Δx =200m in this study, thus Δy = 173 m and Δz = 100 m for the dip angle of 30°. A finer mesh size of 100 m is tested for comparison with 200 m by Meng et al. (2022) using similar model parameters, and suggests that results simulated with 200 m mesh

size is robust. Other model parameters are shown in Table 1.

The main fault dimension is 120 km along strike and 40 km along dip, which is surrounded by creeping zones with velocity strengthening property (Figure 1). Distributions of main parameters, such as a, b, L, σ , velocity and density over the main fault are shown in Figure 2. We set up two asperities Z1 and Z2 over the largely conditionally stable thrust fault. Over the conditionally stable zone, where spontaneous SSEs could occur, a-b=-0.002, L=4mm and initial $\bar{\sigma}_n$ =20 MPa. On Z1 asperity, a-b=-0.004, L=10 mm and initial $\bar{\sigma}_n=50$ MPa, which we name as a high normal stress (HNS) asperity. On Z2 asperity, a-b=-0.004, L=4mm and initial $\bar{\sigma}_n$ =20 Mpa, which we name as a low normal stress (LNS) asperity. The HNS asperity corresponds to higher effective normal stress on fault interface, which may relate with high-relief topographic highs such as subducted seamounts (Scholz and Small, 1997). The LNS asperity could relate with low-relief topographic highs on the subducting interface. Other mechanisms may also form asperities within a conditionally stable zone, for example some high permeable sediments could more easily get compacted and lithified (Pacheco et al., 1993), compared with low permeable sediments, and generate locally locked patches as asperities. Large tsunami earthquakes could be formed by a cascading rupture over a series of asperities (Bilek and Lay, 2002; Meng et al., 2022), thus we set up two different kinds of asperities to explore their interactions with shallow SSEs in earthquake cycle simulations.

The stability of the fault plane with velocity-weakening property is strongly affected by the critical nucleation size h^* . For the 3D mode II earthquakes h^* can be expressed by (Chen and Lapusta, 2009; Rubin and Ampuero, 2005):

171
$$h^* = \frac{\pi}{2} \frac{\mu b L}{(1 - \nu)(a - b)^2 \overline{\sigma}_n}$$
 (3)

149

150

151

152

153

154

155

156

157

158

159

160

161

162

163

164

165

166

167

168

169

170

172

173

where μ and ν are shear modulus and Poisson's ratio, shown in Table 1, respectively. In our model, the h^* on Z1 and Z2 asperities are about 13 km in dimension (Supporting Information Figure S1), smaller than the size of Z1 and Z2, which is about 14 by 14 km. Thus, earthquakes can nucleate on these two asperities. However, h^* on the conditionally stable zone (velocity weakening zone surrounding Z1 and Z2) is about 50 km (Supporting Information Figure S1), larger than the width of the conditionally zone, about 25 km. Thus, earthquakes can only nucleate on Z1 and Z2 asperities, but could propagate onto the conditionally stable zone.

The earthquake cycle simulation starts from an interseismic phase by setting up the on-fault initial effective normal stress $\bar{\sigma}_n$ (Figure 2), the initial slip rate $V_{ini} = V_{pl}$, the initial steady state variable $\theta_{ini} = L/V_{ini}$ and the corresponding initial steady state shear stress $\tau_{ini} = \bar{\sigma}_n * [f_0 + (a - b) * ln \frac{V_{ini}}{V_0}]$. To initialize the simulation, we set up an artificial nucleation patch (within Z1 asperity) with a lower initial slip rate $V_{ini} = V_{pl} * 0.05$, which will impose a higher initial steady-state shear stress within the nucleation patch compared with surrounding area (Luo et al., 2020).

3. Results:

We perform a multicycle dynamic simulation on the model for 220 years. Figure 3a shows slip behaviors and event patterns during this period with maximum slip rates. Slip rate peaks on the order of \sim 1 m/s (seismic rate) correspond to earthquakes and those above V_{pl} (10⁻⁹ m/s) but below seismic rates represent SSEs. We consider a rupture of the two asperities as one earthquake, even though the rupture may pause for a certain time (up to hundreds of seconds) before it breaks the second asperity. One feature in the event patten from this model is that a small event (Type I) that ruptures only the LNS asperity (Z2) and a big earthquake (Type II) that ruptures both asperities (Z1 and Z2) alternatively occur on the fault (Table 2). These earthquakes nucleate on one of the two asperities and propagate slowly into the surrounding conditionally stable

zone. The most striking feature in this model is the correlation between the size of an earthquake and the activity of SSEs preceding the earthquake. Type II earthquake is preceded by an interseismic period with active SSEs, while a Type I earthquake is preceded by a relatively quiet interseismic period with few SSEs (Table 2). A related but different feature is that SSEs occur soon after a Type I earthquake, while SSEs do not occur after Type II earthquake until the late stage of the following interseismic period (Figure 3).

Figure 3b shows these features in more details for the time period between the 105th and 170th years into the simulation. After Event 1 (Type I), SSEs start to occur at a recurrence interval of ~6 years regularly. The following earthquake Event 2 (Type II) is preceded by six SSEs, marking a very active interseismic period (Interseismic 1). After Event 2, SSEs are absent in the following ~20 years and only occur once during the late stage of the interseismic period (Interseismic 2). Then, Event 3 (Type I) is only preceded by one SSE at the late stage of Interseismic 2. These results suggest strong interactions between shallow SSEs and subduction earthquakes.

To explore effects of the six SSEs on Event 2 (Type II), we plot slip rate snapshots, cumulative shear stress change and slip distributions during each SSE in Figure 4. The slip rate and accumulated slip, which are the kinematic quantities, show that SSEs all occur over the conditionally stable zone. The first four SSEs (S1-S4) occur mainly to the left of the Z1 asperity. The fifth SSE (S5) occurs both to the left of Z1 and to the right of Z2, ending the locking status to the right of Z2. The sixth SSE (S6) produces slip mainly between two asperities, ending the locking status of this zone. Generally, the locked area (of low slip rate < 10^{-10} m/s) becomes smaller and smaller as consecutive SSEs occur (left panels in Figure 4). Shear stress change (middle panels), which is a dynamic quantity, shows stress drop is associated with slip areas of SSEs, and stress

increase is associated with locked areas during each SSE. We also calculate the normal stress change and Coulomb stress change assuming an apparent friction of 0.4, during each SSE (Supporting Information Figure S2). Because the normal stress change is much smaller than shear stress change during an interseismic period, we only discuss shear stress change in this study. We further analyze the stress evolution during Interseismic 1 to reveal how SSEs affect the stress states over the fault plane. We analyze the stress evolution history for multiple points along a horizontal profile (20 km along dip, Figure 5). Time histories of points F1-F7 over the left boundary of Z1 show that the successive SSEs (S1-S5) gradually load shear stress to the interior of the high-strength asperity Z1 (Figure 6a). F1-F7 are on the slope from the surrounding area with low normal stress (~20 MPa at F1) to high normal stress (~50 MPa at F7) on Z1 (Figure 5). As shown in Figure 6a, the first SSE S1 ruptures F1 and causes a steep shear stress increase at F2. S2 ruptures F1-F3 and loads F4 obviously. S3 ruptures F1-F4 and clearly loads F5. S4 ruptures F1-F5 and loads shear stress of more than 3 MPa to F6. S5 ruptures F1-F6 and loads F7 significantly. Tectonic loading (V_{pl}) , transferred as elastic stress through the media of the hanging wall and footwall, may also contribute to shear stress increase at much lower rates, evidenced by the fact that shear stress increases slowly before SSE arrivals, which can be clearly seen at point F3-F7. However, stress loading from SSEs is more efficient (e.g., higher rates with steeper slopes in Figure 6a) than tectonic loading. Points G1-G7 locate at the right boundary of low normal stress (LNS) asperity Z2, and they are only affected by SSE S5 at the late stage of Interseismic 1(Figure 6b) in addition to tectonic loading. Because these points locate near a low strength asperity, S5 caused stress perturbation on these points almost at the same time, without a

224

225

226

227

228

229

230

231

232

233

234

235

236

237

238

239

240

241

242

243

244

245

246

248 migration process observed at points F1-F7, implying that stress within Z2 asperity is 249 easily influenced by SSEs. 250 In the conditionally stable zone, points A-E experience small stress perturbation (~1 251 MPa) periodically at every 5-6 years, corresponding to the influence of SSE S1-S5 252 (Figure 6c). However, for points H-L, before SSE S5 most of the conditionally stable zone in this area is locked with low slip rate < 10⁻¹⁰ m/s (Figure 4). The stress 253 perturbation advances from the right side (L) to the left side (H) over Interseismic 1 254 255 (Figure 6d) slowly. The migrating speed accelerates from <0.5 km/year to >4km/year, 256 until SSE S5 fully develops at around 133 year. This may reflect that a conditionally 257 stable zone takes a long time to turn from a locked status to a unlocked status, after that 258 SSE can form in such a zone. 259 Figure 7 shows shear stress change and slip distributions on the fault plane during 260 the two events (Event 1 and Event 2) and the following postseismic and interseismic 261 periods. Rupture time contours are also shown for the coseismic process of the two 262 events. Both dynamic events nucleate on the LNS asperity Z2 and propagate slowly (< 263 1.5 km/s, Figure 7a and 7d) into the surrounding conditional stable zone. Event 1 stops 264 at the HNS asperity Z1 with slip distribution on the right half of the fault plane and moment magnitude of Mw 7.07 (Table 2). The rupture in Event 2 pauses about 55 s 265 266 (Figure 3b and Figure 7d) when it encounters the HNZ asperity Z1 but finally breaks 267 Z1, resulting in a larger event (Mw 7.32) with slip distribution on the entire fault plane 268 (Table 2). A HNZ asperity can be difficult to get ruptured during a cascading event 269 (Type II) and causes abnormally long duration, for example the total duration for Event

2 is longer than 100 s (Figure 7d). If the rupture speed is calculated based on distance

divided by duration, Event 2 has a much slower average rupture speed ~0.7 km/s,

further contributing to the characteristics of slow rupture speed of tsunami earthquakes.

270

271

The final ground surface displacement and continuous seismic waveforms for Event 1 and 2 are displayed in Figure S4 and S5 (Supporting Information), suggesting a maximum ground surface displacement of ~ 0.8 m for a Mw 7.3 Type II earthquake and ~ 0.5 m for a Mw 7.1 Type I earthquake (centroid depth ~ 10 km), in this study. The features of exceptionally slow rupture speed, long duration and non-neglectable ground surface displacement are consistent with observed tsunami earthquake characters. Afterslip mainly occurs near the free surface during the following postseismic periods after both events (Figure 7b and 7e) due to velocity strengthening behavior there (Figure 1b).

During Interseismic 2, only one SSE S7 fully develops at the late stage to the right of the fault plane (Supporting Information Figure S3). There is an absence of SSE activity during the early stage of Interseismic 2, because Event 2 ruptures the whole fault plane and generates stress drop in the conditionally stable zone (Figure 7d), which needs a long time of shear stress accumulation to reach the strength for later SSE rupture. It is similar to the absence of SSE activity to the right of fault plane during Interseismic 1, for example in points H-L (Figure 6d). Event 3 occurs more than 7 years later after SSE S7, suggesting S7 does not directly cause nucleation of Event 3 (Supporting Information Figure S6). The movie of slip rate evolution from Event 1 to Event 3 (~60 years) for the whole fault plane is provided in Supplemental Materials.

4. Discussion

In our two-asperities model, a large earthquake (Type II) that ruptures both the LNS and HNS asperities is preceded by an interseismic period with periodic, active SSEs, while a small earthquake (Type I) that ruptures only the LNS asperity is preceded by a relatively quiet interseismic period with fewer SSEs. It appears that active SSEs prime

an HNS asperity for failure in a future earthquake. Without enough stress loading from active SSEs surrounding an HNS, the HNS more likely acts as a barrier in the next earthquake rupture. Therefore, for a subduction zone with some HNS asperities (such as topographic highs on the subduction interface) identified, active SSEs may suggest a larger earthquake (Type II) may follow, compared with the case with few SSEs. After the earthquake nucleates on asperities and propagates into the conditionally stable zone, the rupture speed could be significantly slowed down (<1.5 km/s), generating a long source duration, which corresponds to the characteristics of shallow tsunami earthquakes. The shallow conditionally stable zone is a potential factor leading to tsunami earthquakes (Bilek and Lay, 2002; Meng et al., 2022), so that monitoring and studying the interaction of shallow SSE and earthquakes could be essential for assessing the hazard of tsunami earthquake at shallow subduction zones.

Our results show that in some cases, an SSE may directly lead to the nucleation of an earthquake (e.g., S6 leading to Event 2), while in other cases, an SSE may not directly contribute to the nucleation of next earthquake (e.g., S7 versus Event 3). These findings are consistent with recent observations reviewed in Introduction. Our physics-based models suggests that whether or not an SSE, occurring in a conditionally stable zone, leads to nucleation of an earthquake depends on if nearby asperities (velocity-weakening patches) are ready (in terms of stress condition) for spontaneously dynamic rupture.

Our results suggest that the coupling degree of a conditionally stable patch may vary significantly between different interseismic periods (Figure 8), due to different levels of SSE activities. The coupling degree here is defined as $1 - \frac{s}{V_{pl}*T}$, where S is the fault slip over a time period of T and V_{pl} is the relative loading rate between the footwall and hanging wall applied in our model (Figure 1 and Table 1). Therefore, without

considering the history of earthquakes and SSEs over multiple earthquake cycles, the coupling degree estimated from geodetic surveys within one earthquake cycle may be misleading. It appears that the readiness of high strength asperities (such as topographic highs) on a shallow subduction interface dominates sizes of shallow tsunami earthquakes.

In this study, we focus on the studying the interactions between SSEs and earthquakes. In our model, ruptures that nucleate on an asperity could continue propagating onto the surrounding conditionally stable zone, generating earthquakes with characteristics resembling tsunami earthquakes. These ruptures can interact with SSEs mainly occurring in the conditionally stable zone, as shown in the 2011 Tohoku-Oki earthquake, 2012 Iquique earthquake, and probably also the two 1947 Hikurangi tsunami earthquakes. To further test this predictive model, we need more long-term offshore geodetic observations to precisely locate shallow SSEs and study their interactions with shallow earthquakes through earthquake cycles, especially for regions near historical tsunami earthquakes. We remark that there are some subduction zone observations suggesting that interactions between megathrust earthquakes and deep SSEs could be weak, For example, the SSE recurrence interval stays unchanged before and after the 2014 Mw 7.6 Nicoya earthquake (Xie et al., 2020). We speculate that the stress condition and friction parameters in this case is very different from our model. For example, there may be a large velocity-strengthening zone separating SSE zones and the 2014 earthquake rupture area. Furthmore, to study a specific subduction zone in the future, for example the Hikurangi or Nicoya margin, one will need to explore a large parameter space to match the seismic and geodetic observations for the specific margin.

347

323

324

325

326

327

328

329

330

331

332

333

334

335

336

337

338

339

340

341

342

343

344

345

5. Conclusions

Our physics-based models show that SSEs and shallow subduction zone earthquake ruptures may collocate on a fault plane. High-strength asperities can be effectively loaded by successive SSEs, in addition to tectonic loading, priming them for failure that leads to a large earthquake that ruptures the entire fault plane. The interseismic coupling degree could be low preceding a large earthquake due to active SSEs, but becomes high preceding a small earthquake due to much fewer preceding SSEs. The identification and characterization of both shallow asperities and SSEs are important for earthquake and tsunami hazard assessment and reduction along subduction zones.

Data and Resources:

In this study, the simulation results are generated from our computer simulation model and no data were used from other resources. The figures and movie, shown in the main text and supplemental files, are plotted with MATLAB (http://www.mathworks.com/) software. The movie showing slip-rate evolution from Event 1 to Event 3 is provided as electronic supplemental file. Six figures (Figure S1-S6) are included in a supplemental document. Figure S1 shows the distribution of critical nucleation size h* over the fault plane and along three profiles, Figure S2 normal stress change, shear stress change and Coulomb stress change for six SSEs S1-S6, Figure S3 shows the slip rate, stress change and slip distribution for SSE S7, Figure S4 and S5 are ground surface displacements for Event 1 and 2 and Figure S6 shows the stress change and slip distribution for Event 3.

373 **Acknowledgement:**

- 374 This study is supported by NSF grants EAR-2013695 and EAR-2147340, and
- 375 Gangi/Heep professorship in theoretical geophysics from the College of Geosciences
- 376 at Texas A&M University. The authors appreciate High Performance Research
- 377 Computing at Texas A&M University (https://hptc.tamu.edu) for providing the
- advanced computer resources used in this study.

379

380

References:

- 381 Ammon, C. J., H. Kanamori, T. Lay, and A. A. Velasco (2006), The 17 July 2006 Java
- tsunami earthquake, Geophys. Res. Lett., 33, L24308, doi:10.1029/2006GL028005.
- 383 Abercrombie, R. E., M. Antolik, K. Felzer, and G. Ekström (2001), The 1994 Java
- tsunami earthquake: Slip over a subducting seamount, J. Geophys. Res., 106, 6595–
- 385 6607, doi:10.1029/2000JB900403.
- 386 Bell, R., C. Holden, W. Power, X. Wang, and G. Downes (2014), Hikurangi margin
- tsunami earthquake generated by slow seismic rupture over a subducted seamount,
- 388 Earth Planet. Sci. Lett., 397, 1–9.
- 389 Bilek, S.L., Lay, T. (2002), Tsunami earthquakes possibly widespread manifestations
- of frictional conditional stability. Geophysical Research Letters 29, 18-1-18-4...
- 391 doi:10.1029/2002gl015215
- 392 Chen, T., and N. Lapusta (2009), Scaling of small repeating earthquakes explained by
- interaction of seismic and aseismic slip in a rate and state fault model, J. Geophys.
- Res. Solid Earth, 114(B1), doi:10.1029/2008JB005749.
- 395 Dieterich, J. H. (1979), Modeling of rock friction: 1. Experimental results and
- 396 constitutive equations, J. Geophys. Res., 84(B5), 2161-2168,
- 397 doi:10.1029/JB084iB05p02161.

- 398 Dixon, T.H., Jiang, Y., Malservisi, R., Mccaffrey, R., Voss, N., Protti, M., Gonzalez,
- V. (2014), Earthquake and tsunami forecasts: Relation of slow slip events to
- subsequent earthquake rupture. Proceedings of the National Academy of Sciences
- 401 111, 17039–17044.. doi:10.1073/pnas.1412299111.
- 402 Douglas, A., J. Beavan, L. Wallace, and J. Townend (2005), Slow slip on the northern
- Hikurangi subduction interface, New Zealand, Geophys. Res. Let t., 32, L16305,
- 404 doi:10.1029/2005GL023607.
- Dragert, H., Wang, K., & James, T. S. (2001). A silent slip event on the deeper Cascadia
- 406 subduction interface. Science, 292(5521), 1525–1528.
- 407 Duan, B. (2012), Dynamic rupture of the 2011 Mw 9.0 Tohoku-Oki earthquake: Roles
- of a possible subducting seamount, J. Geophys. Res., 117(B5),
- 409 doi:10.1029/2011JB009124.
- Duan, B. (2010), Role of initial stress rotations in rupture dynamics and ground motion:
- A case study with implications for the Wenchuan earthquake, J. Geophys. Res. Solid
- 412 Earth, 115(B5), doi:10.1029/2009JB006750.
- Duan, B., and S. M. Day (2008), Inelastic strain distribution and seismic radiation from
- rupture of a fault kink, J. Geophys. Res., 113(B12), doi:10.1029/2008JB005847.
- Duan, B., and D. D. Oglesby (2006), Heterogeneous fa 734 ult stresses from previous
- earthquakes and the effect on dynamics of parallel strike-slip faults, J. Geophys. Res.,
- 417 111(B5), doi:10.1029/2005JB004138.
- 418 Erickson, B. A., and E. M. Dunham (2014), An efficient numerical method for
- earthquake cycles in heterogeneous media: Alternating subbasin and surface-
- rupturing events on faults crossing a sedimentary basin, J. Geophys. Res. Solid Earth,
- 421 119(4), 3290-3316, doi:10.1002/2013JB010614.

- 422 Franco, S., Kostoglodov, V., Larson, K., Manea, V., Manea, M., & Santiago, J. (2005).
- Propagation of the 2001–2002 silent earthquake and interplate coupling in the
- Oaxaca subduction zone, Mexico. Earth Planets Space, 57(10), 973–985.
- 425 Ghosh, A., Huesca-Pérez, E., Brodsky, E., Ito, Y., 2015. Very low frequency
- earthquakes in Cascadia migrate with tremor. Geophysical Research Letters 42,
- 427 3228–3232, doi:10.1002/2015gl063286.
- 428 Hirose, H., Hirahara, K., Kimata, F., Fujii, N., & Miyazaki, S. (1999). A slow thrust
- slip event following the two 1996 Hyuganada earthquakes beneath the Bungo
- Channel, Southwest Japan. Geophysical Research Letters, 26(21), 3237–3240.
- 431 Hirose, Hitoshi, Hisanori Kimura, Bogdan Enescu, and Shin Aoi. (2012). Recurrent
- slow slip event likely hastened by the 2011 Tohoku earthquake. Proceedings of the
- National Academy of Sciences 109. Proceedings of the National Academy of
- 434 Sciences: 15157–15161. doi:10.1073/pnas.1202709109.
- Hughes, T. J. (2000), The Finite Element Method: Linear Static and Dynamic Finite
- 436 Element Analysis, Courier Corporation.
- 437 Ito, Y., Obara, K., Shiomi, K., Sekine, S., Hirose, H., 2007. Slow Earthquakes
- Coincident with Episodic Tremors and Slow Slip Events. Science 315, 503–506,
- 439 doi:10.1126/science.1134454.
- Ito, Y., Obara, K., Matsuzawa, T. & Maeda, T. (2009), Very low frequency earthquakes
- related to small asperities on the plate boundary interface at the locked to aseismic
- transition. J. Geophys. Res. 114, B00A13
- Ito, Y., et al. (2013), Episodic slow slip events in the Japan subduction zone before the
- 444 2011 Tohoku-Oki earthquake, Tectonophysics, 600, 14–26,
- 445 doi:10.1016/j.tecto.2012.08.022.

- Kanamori, H. (1972), Mechanism of tsunami earthquakes, Phys. Earth Planet. Inter., 6,
- 447 346–359, doi:10.1016/0031-9201(72)90058-1.

- Kanamori, H., and M. Kikuchi (1993), The 1992 Nicaragua earthquake: A slow tsunami
- earthquake associated with subducted sediments, Nature, 361, 714–716,
- 451 doi:10.1038/361714a0.
- 452 Kao, H., Wang, K., Dragert, H., Rogers, G. C. & Kao, J. Y. (2009), Large contrast
- between the moment magnitude of tremor and the moment magnitude of slip in
- 454 ETS events. Eos 90 (suppl.), T22B-04.
- 455 Kato, A., K. Obara, T. Igarashi, H. Tsuruoka, S. Nakagawa and N. Hirata (2012).
- 456 "Propagation of slow slip leading up to the 2011 M(w) 9.0 Tohoku-Oki
- 457 earthquake." <u>Science</u> 335(6069): 705-708.
- 458 Lay, T., C. J. Ammon, H. Kanamori, Y. Yamazaki, K. F. Cheung, and A. R. Hutko
- 459 (2011), The 25 October 2010 Mentawai tsunami earthquake (Mw 7.8) and the
- 460 tsunami hazard presented by shallow megathrust ruptures, Geophys. Res. Lett.,
- 461 38, L06302, doi:10.1029/2010GL046552.
- Linde, A. T., M. T. Gladwin, M. J. S. Johnston, R. L. Gwyther, and R. G. Bilham
- 463 (1996), A slow earthquake sequence on the San Andreas fault, Nature, 383(6595),
- 464 65–68, doi:10.1038/383065a0.
- Lowry, A. R., Larson, K.M., Kostoglodov, V., & Bilham, R. (2001). Transient fault slip
- in Guerrero, SouthernMexico. Geophysical Research Letters, 28(19), 3753–3756.
- 467 https://doi.org/10.1029/2001GL013238.
- Lapusta, N., and Y. Liu (2009), Three-dimensional boundary integral modeling of
- spontaneous earthquake sequences and aseismic slip, J. Geophys. Res. Solid Earth,
- 470 114(B9), doi:10.1029/2008JB005934.

- Lapusta, N., J. R. Rice, Y. Ben-Zion, and G. Zheng (2000), Elastodynamic analysis for
- slow tectonic loading with spontaneous rupture episodes on faults with rate-and
- state-dependent friction, J. Geophys. Res., 105(B10), 23765-23789,
- 474 doi:10.1029/2000JB900250.
- Li, D. and Y. Liu (2016). Spatiotemporal evolution of slow slip events in a nonplanar.
- fault model for northern Cascadia subduction zone. <u>Journal of Geophysical</u>
- 477 <u>Research: Solid Earth</u> 121(9): 6828-6845.
- Liu, Y. and J. R. Rice (2005). Assismic slip transients emerge spontaneously in three
- dimensional rate and state modeling of subduction earthquake sequences. <u>Journal of</u>
- 480 <u>Geophysical Research: Solid Earth</u> 110(B8).
- Liu, D., and B. Duan (2018), Scenario Earthquake and Ground-Motion Simulations in
- North China: Effects of Heterogeneous Fault Stress and 3D Basin Structure, Bull.
- 483 Seismol. Soc. Am., doi:10.1785/0120170374.
- 484 Luo, B., and B. Duan (2018), Dynamics of Non-planar Thrust Faults Governed by
- Various Friction Laws, J. Geophys. Res. Solid Earth, doi:10.1029/2017JB015320.
- 486 Luo, B., Duan, B., and Liu, D. (2020), 3D Finite-Element Modeling of Dynamic
- Rupture and Aseismic Slip over Earthquake Cycles on Geometrically Complex
- Faults. Bulletin of the Seismological Society of America, 110, 2619–2637,
- 489 doi:10.1785/0120200047.
- 490 Meng, Q., B. Duan, and B. Luo (2022), Using a dynamic earthquake simulator to
- explore tsunami earthquake generation. Geophysical Journal International 229, 255–
- 492 273.. doi:10.1093/gji/ggab470
- 493 Obara, K. (2002), Nonvolcanic deep tremor associated with subduction in southwest
- 494 Japan. Science 296, 1679–1681.

- 495 Ozawa, S., S. Miyazaki, Y. Hatanaka, T. Imakiire, M. Kaidzu, and M. Murakami
- 496 (2003), Characteristic silent earthquakes in the eastern part of the Boso peninsula,
- 497 Central Japan, Geophys. Res. Lett., 30, doi:10.1029/2002GL016665.
- 498 Ozawa, S., Suito, H., Tobita, M., 2007. Occurrence of quasi-periodic slow-slip off the
- east coast of the Boso peninsula, Central Japan. Earth, Planets and Space 59, 1241–
- 500 1245, doi:10.1186/bf03352072.
- Peng, Z. & Gomberg, J. (2010), An integrated perspective of the continuum between
- earthquakes and slow-slip phenomena. Nature Geosci. 3, 599–607.
- Qiang, S. (1988), An adaptive dynamic relaxation method for nonlinear problems,
- 504 Computers & Structures, 30(4), 855-859.
- Rubin, A.M., and Ampuero, J.-P. (2005). Earthquake nucleation on (aging) rate and
- state faults. Journal of Geophysical Research: Atmospheres 110..
- 507 doi:10.1029/2005jb003686.
- Rogers, G. and H. Dragert (2003). Episodic tremor and slip on the Cascadia subduction
- zone: the chatter of silent slip. <u>Science</u> 300(5627): 1942-1943.
- Ruiz, S., Metois, M., Fuenzalida, A., Ruiz, J., Leyton, F., Grandin, R., et al. (2014).
- Intense foreshocks and a slow slip event preceded the 2014 Iquique Mw 8.1
- 512 earthquake. Science, 345(6201), 1165–1169.
- 513 https://doi.org/10.1126/science.1256074
- 514 Saffer, D.M., Wallace, L.M. (2015), The frictional, hydrologic, metamorphic and
- thermal habitat of shallow slow earthquakes. Nature Geoscience 8, 594–600...
- 516 doi:10.1038/ngeo2490.
- 517 Segall, P., A. M. Rubin, A. M. Bradley and J. R. Rice (2010). "Dilatant strengthening
- as a mechanism for slow slip events." <u>Journal of Geophysical Research</u> 115(B12).

- 519 Scholz, C. H., and C. Small (1997), The effect of seamount subduction on seismic
- 520 coupling, Geology, 25, 487–490, doi:10.1130/0091-
- 521 7613(1997)025<0487:TEOSSO>2.3.CO;2.
- 522 Shibazaki, B., Wallace, L.M., Kaneko, Y., Hamling, I., Ito, Y. and Matsuzawa, T.,
- 523 2019. Three-Dimensional Modeling of Spontaneous and Triggered Slow-Slip Events
- at the Hikurangi Subduction Zone, NewZealand. Journal of Geophysical Research:
- 525 Solid Earth, 124(12), pp.13250-13268.
- 526 Szeliga, W., Melbourne, T., Santillan, M., Miller, M., 2008. GPS constraints on 34 slow
- slip events within the Cascadia subduction zone, 1997–2005. Journal of Geophysical
- Research: Atmospheres 113.. doi:10.1029/2007jb004948.
- 529 Thomas, M.Y., Lapusta, N., Noda, H., Avouac, J., 2014. Quasi-dynamic versus fully
- dynamic simulations of earthquakes and aseismic slip with and without enhanced
- coseismic weakening. Journal of Geophysical Research: Solid Earth 119, 1986-
- 532 2004.. doi:10.1002/2013jb010615.
- Vallee, M., Nocquet, J.-M., Battaglia, J., Font, Y., Segovia, M., Regnier, M., et al.
- 534 (2013). Intense interface seismicity triggered by a shallow slow slip event in the
- central Ecuador subduction zone. Journal of Geophysical Research: Solid Earth, 118,
- 536 2965–2981.https://doi.org/10.1002/jgrb.50216.
- Wallace, L. M., Beavan, J., Bannister, S. & Williams, C. (2012), Simultaneous long-
- term and short-term slow slip events at the Hikurangi subduction margin, New
- 539 Zealand: implications for processes that control slow slip event occurrence, duration,
- and migration. J. Geophys. Res. 117, B11402.
- Wallace, L.M., Kaneko, Y., Hreinsdóttir, S., Hamling, I., Peng, Z., Bartlow, N.,
- D'Anastasio, E., Fry, B., 2017. Large-scale dynamic triggering of shallow slow slip

543	enhanced by overlying sedimentary wedge. Nature Geoscience 10, 765–770,							
544	doi:10.1038/ngeo3021.							
545	Wei, M., Kaneko, Y., Shi, P., & Liu, Y. (2018). Numerical modeling of dynamically							
546	triggered shallow slow slip events in New Zealand by the 2016 Mw 7.8 Kaikoura							
547	earthquake. Geophysical Research Letters, 45, 4764-4772.							
548	https://doi.org/10.1029/2018GL077879							
549	Xie, S., Dixon, T. H., Malservisi, R., Jiang, Y., Protti, M., & Muller, C. (2020). Slow							
550	slip and Inter-transient locking on the Nicoya megathrust in the late and early							
551	stages of an earthquake cycle. Journal of Geophysical Research: Solid Earth, 125,							
552	e2020JB020503. https://doi.org/10.1029/2020JB020503							
553	Yu, H., Y. Liu, H. Yang, and J. Ning (2018), Modeling earthquake sequences along the							
554	Manila subduction zone: Effects of three-dimensional fault geometry,							
555	Tectonophysics, doi:10.1016/j.tecto.2018.01.025.							
556								
557								
558								
559	Author Information							
560								
561	Qingjun Meng ¹							
562	E-mail: qimeng@tamu.edu							
563								
564	Bunchun Duan ¹							
565	E-mail: <u>bduan@tamu.edu</u>							

(1) Center of Tectonophysics, Department of Geology & Geophysics, Texas A&M
 University, College Station, TX 77843, United States

Tables

Table 1. Basic model parameters in this study

Parameters	Value
P wave speed V_p	6000 m/s
S wave speed V_s	3464 m/s
Shear modulus μ	32 GPa
Poisson's ratio ν	0.25
Density ρ	2670 kg/m^3
Reference slip velocity V_0	10^{-6}m/s
Steady state friction coefficient f_0	0.6
Loading rate V_{pl}	10^{-9} m/s
Element edge length in x direction Δx	200 m
Element edge length in y direction Δy	$200*\cos(\phi)$ m
Element edge length in y direction Δz	$200*\sin(\phi)$ m
Time step (dynamic simulation)	0.005 s

Table 2. Characteristics of Type I (small) and Type II (big) earthquakes

Types	Examples	Magnitude	No.	of	No.	of	Ruptured	Recurrence	Ruptured	Average
		(Mw)	precedi	ing	follow	ing	asperities	interval	Length	rupture
			SSEs		SSEs			(years)	(km)	speed
										(km/s)
Type I	Event 1	~ 7.1	1		6		Z2	~ 60	~ 70	~ 1.5
	Event 3									
Type II	Event 2	~ 7.3	6		1		Z1 & Z2	~ 60	~ 110	~ 0.7

List of Figure Captions

Figure 1. Schematic diagram that shows the 3D thrust fault model, with dip angle of 30 degrees, and boundary conditions for the model. Plane 1 (mainly blue) is the main fault with generally velocity-weakening frictional property that can host earthquake ruptures during coseismic period. Two dark blue squares are asperities where earthquakes can nucleate. Plane 2 (green) is of velocity-strengthening property that creeps during interseismic period. Top boundary is free surface. In quasi-static simulation, left and right boundaries are fixed in x-direction, and are free in

other directions. One half of the plate convergence rate (0.5*V_{pl}) is applied to other model 586 587 boundaries for thrust faulting as indicated by the arrows. 588 589 590 Figure 2. (a) Distributions of friction parameters a-b, effective normal stress and critical distance 591 over the fault plane, and cross sections of (b) friction parameters a, b, a-b, (c) material properties, 592 (d) effective normal stress, and (e) critical distance along a profile (dashed line along dip) in (a). 593 594 Figure 3. (a) Evolution of simulated maximum slip rates on the fault over earthquake cycles. Slip 595 rate peaks larger that 0.1 m/s are earthquakes, labeled by the asperities that are ruptured with a possible time delay between two asperities. Slip rates of above 10⁻⁹ m/s but below 0.1 m/s suggest 596 597 slow slip events. (b) The zoom-in time period from 105th to 172th years, including two interseismic 598 periods (long blue double arrows: Interseismic 1 experiences six SSEs S1-S6 and Interseismic 2 only has one SSE S7), three earthquakes (coseismic periods: Event 1 at 108th year and Event 3 at 169th 599 year only rupture Z2 asperity, while Event 2 ruptures both Z1 and Z2 asperities at 138th year), and 600 601 two postseismic periods 1 and 2 (short red double arrows). 603 Figure 4. Slip rate snapshots (left), cumulative shear stress changes (middle), and cumulative slip

602

604

605

606

607

distributions (right) during six SSEs (a) S1 (b) S2 (c) S3 (d) S4 (e) S5 (f) S6 shown in Fig. 3b. The dark blue zones in the left panels and right panels are locked zones. Positive (red) and negative (blue) values in the middle panels correspond to shear stress increase and drop, respectively. The two boxes denote Z1 (left) and Z2 (right) asperities.

608

609

610

611

612

613

614

Figure 5. Shear stress changes over space and time during Interseismic 1 (shown in Fig. 3b) along a horizontal profile. (a) The initial normal stress distribution on the fault plane. The horizontal profile is shown by the horizontal dashed line at 20 km down-dip distance. Spatial and temporal (with time interval around 1.2 years) shear stress changes along this profile is shown in (b). The Z1 asperity has higher normal stress thus the shear stress over Z1 is also higher than other parts. More detailed temporal shear stress evolution at points A-E, F1-F7, G1-G7 and H-L (illustrated by red

615	dots in (a)) will be shown in Fig. 6. Points F1-F7 and G1-G7 are 0.4 km away from each other.
616	Points A-E and H-L are 5 km away from each other.
617	
618	Figure 6. The temporal shear stress changes during Interseismic 1 (a) at points F1-F7 on the left
619	edge of the Z1 asperity, and (b) at points G1-G7 on the right edge of the Z2 asperity (c) at points
620	A-E in the conditionally stable zone to the left of Z1 asperity (d) at points H-L in the conditionally
621	stable zone to the right of Z2 asperity (see Fig. 5 for locations). The dashed green lines in (a)
622	indicate the shear stress perturbations caused by SSEs S1-S5 on points F1-F7 during Interseismic
623	1. Notice that the scale of shear stress is different.
624	
625	Figure 7. The stress change (top) and slip (bottom) distributions for (a) Event 1 (coseismic), (b)
626	Postseismic 1, (c) Interseismic 1, d) Event 2 (coseismic), (e) Postseismic 2, and (f) Interseismic 2,
627	as illustrated in Fig. 3b. The black boxes denote Z1 (left) and Z2 (right). Rupture times during
628	Event1 and Event 2 are given as contours in (a) and (d), overlaid on color scales of coseismic slip.
629	
630	Figure 8. Coupling degree during the Interseismic periods (a) 1 and (b) 2 ,as shown in Fig. 3b. High
631	or low coupling degree represents strong coupling or weak coupling between the hanging wall and
632	footwall. The black boxes denote the locations of Z1 (left) and Z2 (right) asperities.
633	
634	
635	
636	
637	

Figures:

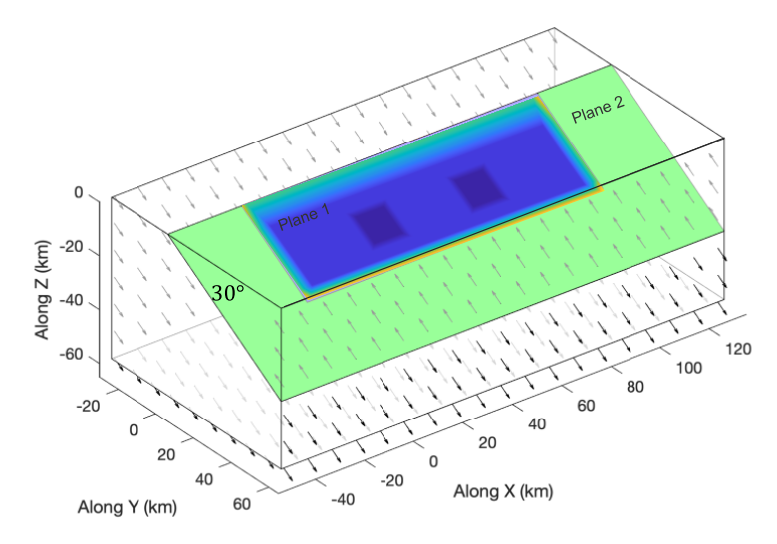


Figure 1. Schematic diagram that shows the 3D thrust fault model, with dip angle of 30 degrees , and boundary conditions for the model. Plane 1 (mainly blue) is the main fault with generally velocity-weakening frictional property that can host earthquake ruptures during coseismic period. Two dark blue squares are asperities where earthquakes can nucleate. Plane 2 (green) is of velocity-strengthening property that creeps during interseismic period. Top boundary is free surface. In quasi-static simulation, left and right boundaries are fixed in x-direction, and are free in other directions. One half of the plate convergence rate $(0.5*V_{\rm pl})$ is applied to other model boundaries for thrust faulting as indicated by the arrows.

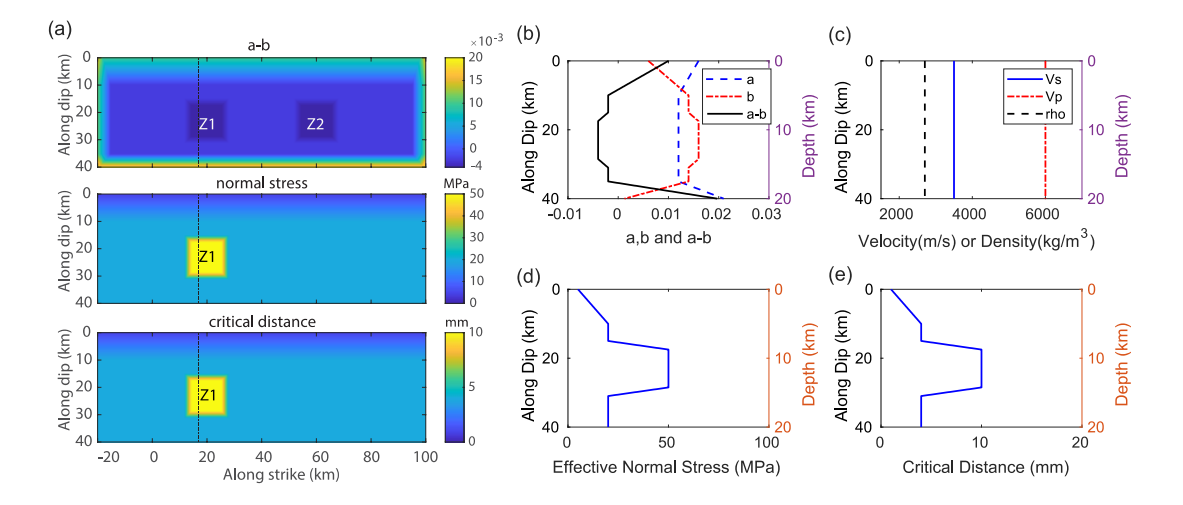


Figure 2. (a) Distributions of friction parameters a-b, effective normal stress and critical distance over the fault plane, and cross sections of (b) friction parameters a, b, a-b, (c) material properties, (d) effective normal stress, and (e) critical distance along a profile (dashed line along dip) in (a).

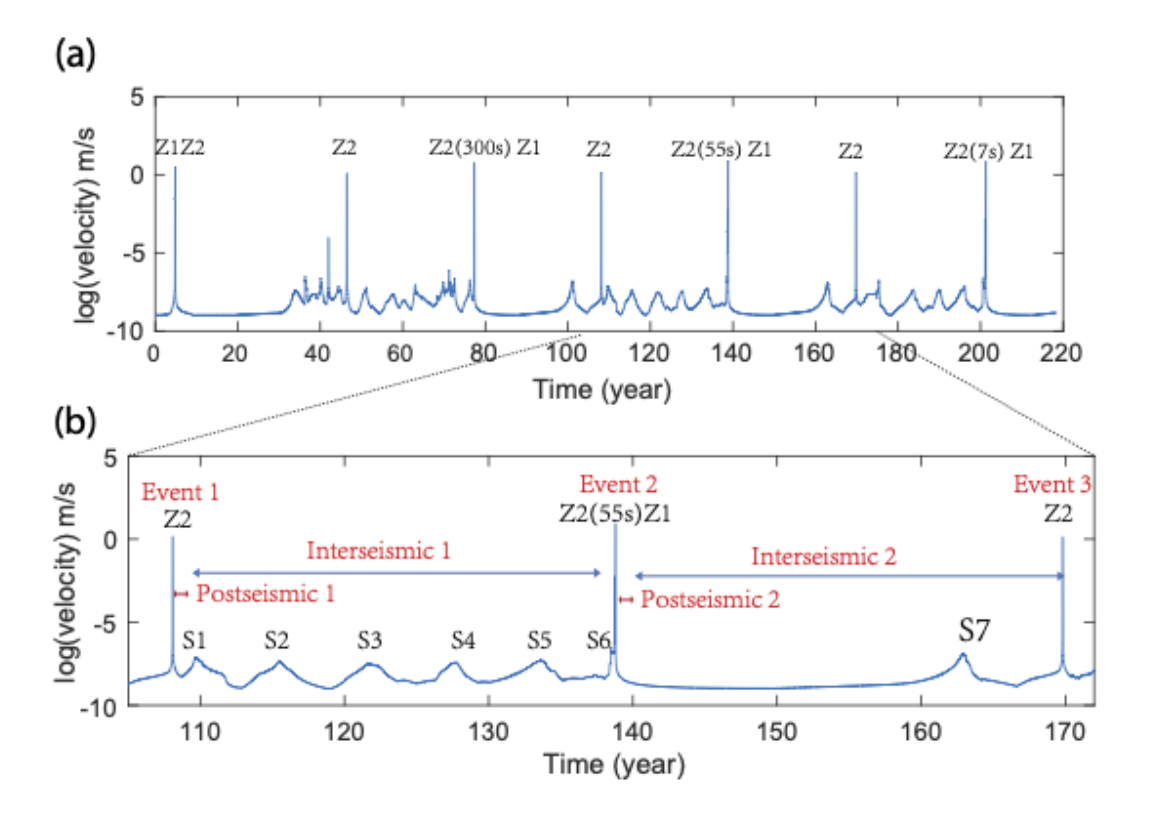


Figure 3. (a) Evolution of simulated maximum slip rates on the fault over earthquake cycles. Slip rate peaks larger that 0.1 m/s are earthquakes, labeled by the asperities that are ruptured with a possible time delay between two asperities. Slip rates of above 10⁻⁹ m/s but below 0.1 m/s suggest slow slip events. (b) The zoom-in time period from 105th to 172th years, including two interseismic periods (long blue double arrows: Interseismic1 experiences six SSEs S1-S6 and Interseismic 2 only has one SSE S7), three earthquakes (coseismic periods: Event 1 at 108th year and Event 3 at 169th year only rupture Z2 asperity, while Event 2 ruptures both Z1 and Z2 asperities at 138th year), and two postseismic periods 1 and 2 (short red double arrows).

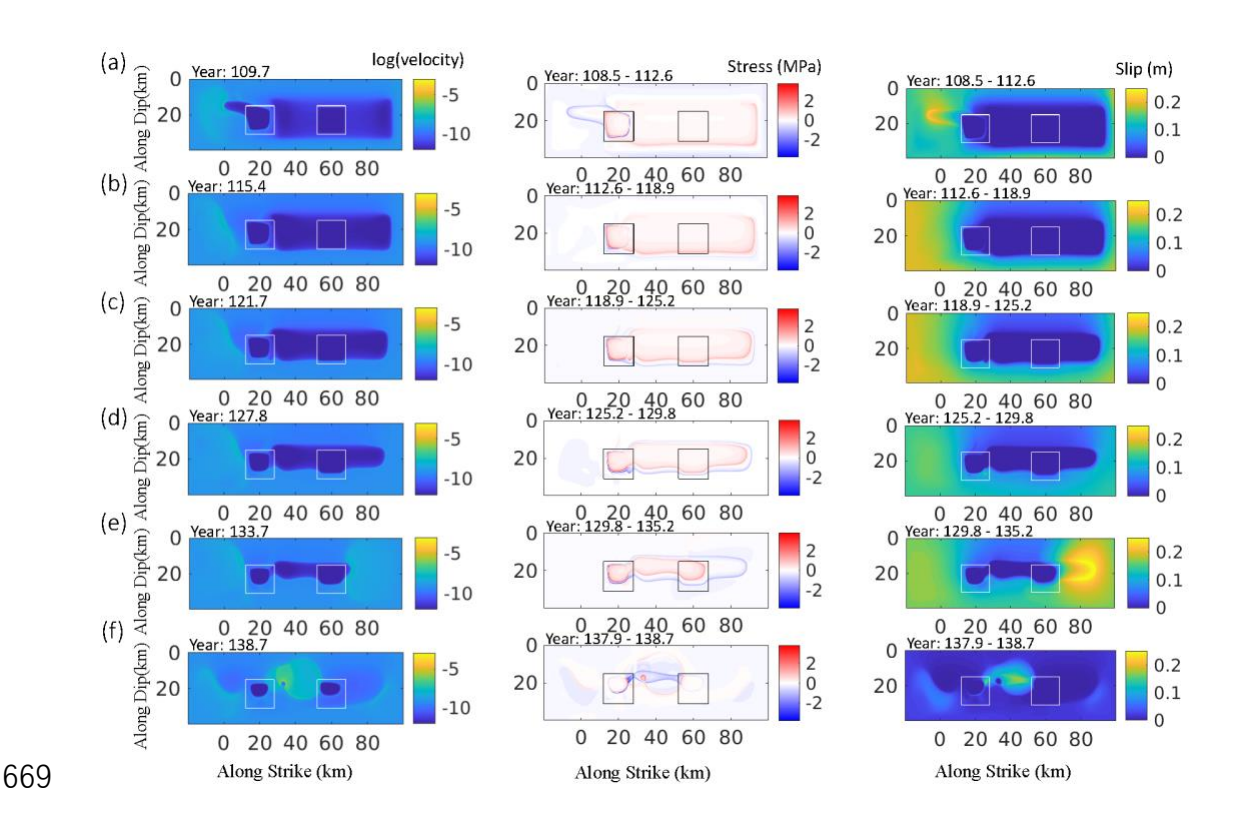


Figure 4. Slip rate snapshots (left), cumulative shear stress changes (middle), and cumulative slip distributions (right) during six SSEs (a) S1 (b) S2 (c) S3 (d) S4 (e) S5 (f) S6 shown in Fig. 3b. The dark blue zones in the left panels and right panels are locked zones. Positive (red) and negative (blue) values in the middle panels correspond to shear stress increase and drop, respectively. The two boxes denote Z1 (left) and Z2 (right) asperities.

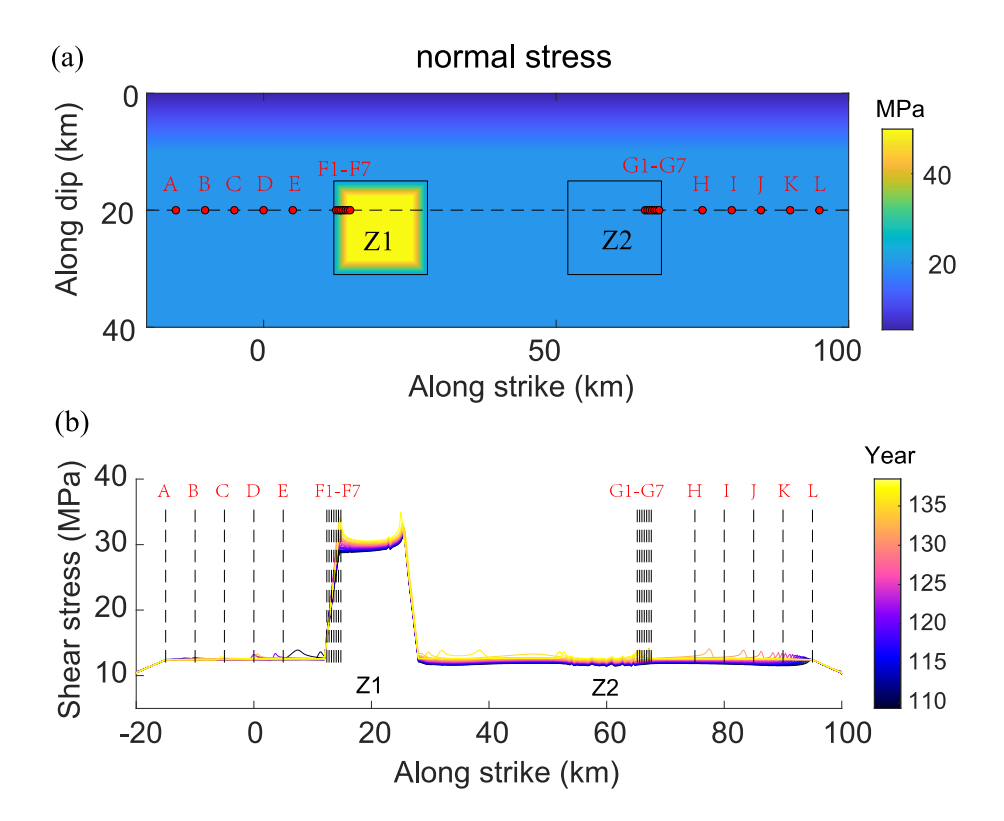


Figure 5. Shear stress changes over space and time during Interseismic 1 (shown in Fig. 3b) along a horizontal profile. (a) The initial normal stress distribution on the fault plane. The horizontal profile is shown by the horizontal dashed line at 20 km down-dip distance. Spatial and temporal (with time interval around 1.2 years) shear stress changes along this profile is shown in (b). The Z1 asperity has higher normal stress thus the shear stress over Z1 is also higher than other parts. More detailed temporal shear stress evolution at points A-E, F1-F7, G1-G7 and H-L (illustrated by red dots in (a)) will be shown in Fig. 6. Points F1-F7 and G1-G7 are 0.4 km away from each other. Points A-E and H-L are 5 km away from each other.

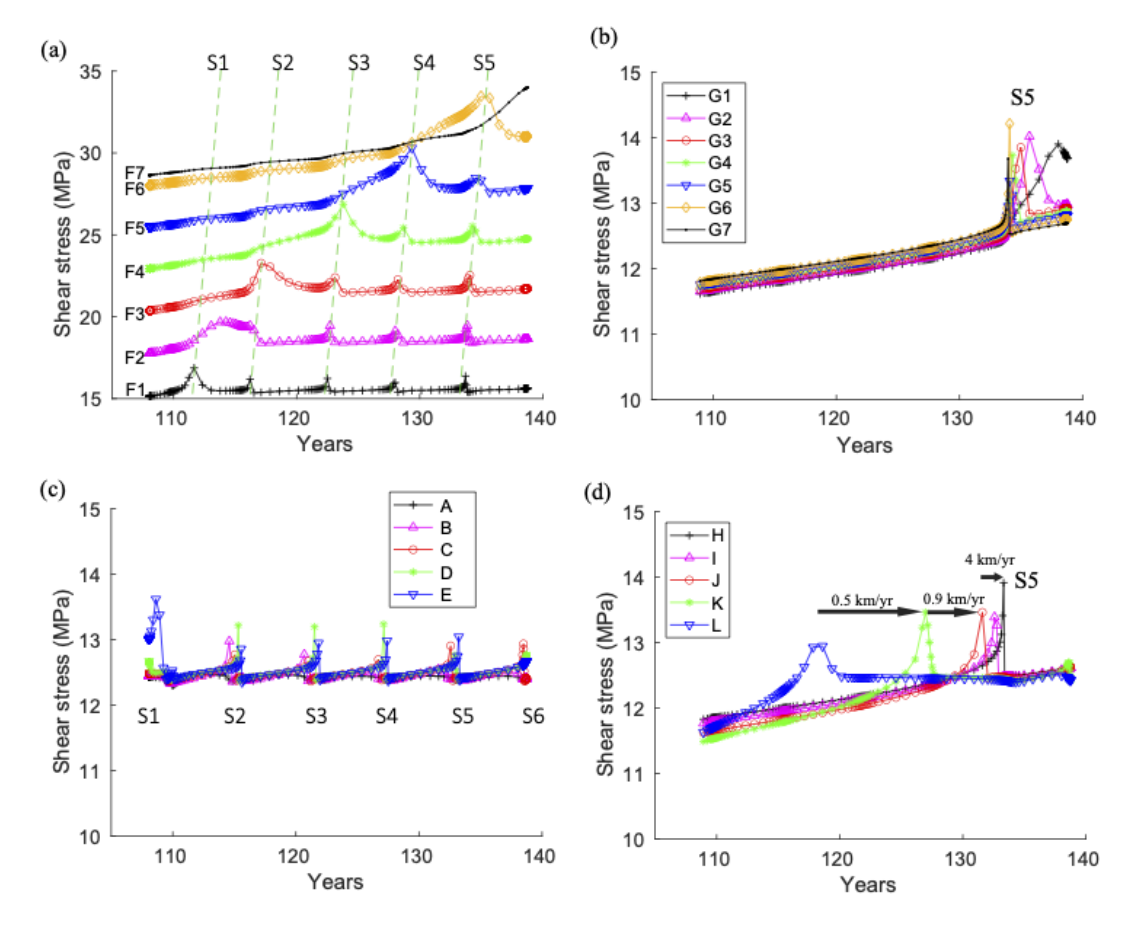


Figure 6. The temporal shear stress changes during Interseismic 1 (a) at points F1-F7 on the left edge of the Z1 asperity, and (b) at points G1-G7 on the right edge of the Z2 asperity (c) at points A-E in the conditionally stable zone to the left of Z1 asperity (d) at points H-L in the conditionally stable zone to the right of Z2 asperity (see Fig. 5 for locations). The dashed green lines in (a) indicate the shear stress perturbations caused by SSEs S1-S5 on points F1-F7 during Interseismic 1. Notice that the scale of shear stress is different.

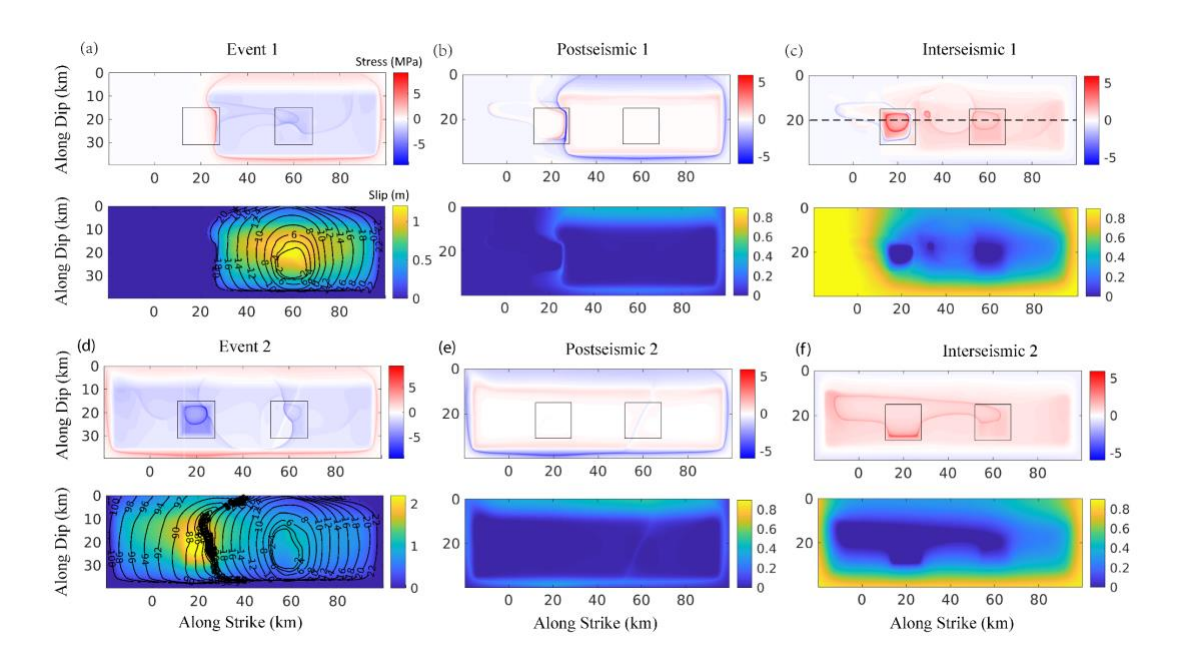


Figure 7. The stress change (top) and slip (bottom) distributions for (a) Event 1 (coseismic), (b) Postseismic 1, (c) Interseismic 1, d) Event 2 (coseismic), (e) Postseismic 2, and (f) Interseismic 2, as illustrated in Fig. 3b. The black boxes denote Z1 (left) and Z2 (right). Rupture times during Event1 and Event 2 are given as contours in (a) and (d), overlaid on color scales of coseismic slip.

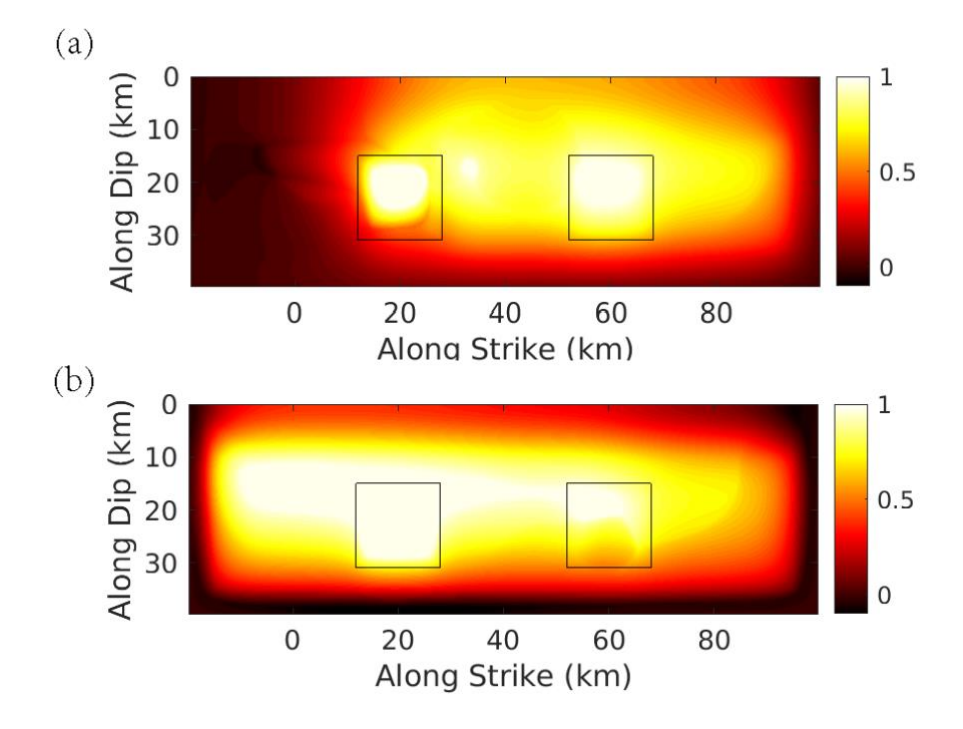


Figure 8. Coupling degree during the Interseismic periods (a) 1 and (b) 2, as shown in Fig. 3b. High or low coupling degree represents strong coupling or weak coupling between the hanging wall and footwall. The black boxes denote the locations of Z1 (left) and Z2 (right) asperities.

712

713